Chapter 31
Biomathematical Modeling of DLGG

Emmanuel Mandonnet

Abstract In this chapter, we review recent advances in biomathematical modeling of glioma growth, based on the proliferation-diffusion equation. We show how the computational simulations from this equation can be compared with real tumor evolution on MRI and how these simulations progressively integrate more realistic anatomical knowledge, improving the accuracy of the virtual tumor evolution. The Achilles' heel of this model comes from the lack of quantitative relation between cell density and abnormal signal on conventional MRI, although future methods could overcome this limitation by taking advantage of multimodal sequences. In its simplified version, the model offers a practical way to monitor tumor dynamics, by estimating the velocity of the tumor front. We also envision applications to the management of DLGG, regarding model-based personalization of treatment sequence and evaluation of treatment efficacy in clinical studies. Finally, we propose a three pathways model of malignant progression. One of this pathway has been mathematically modeled by the proliferation-invasion-hypoxia-necrosis-angiogenesis (PIHNA) system of equations. We show how this model leads to the important concept of kinetics grade, which is complementary to the usual histological grade.

Keywords Biomathematical modeling • Diffuse low-grade glioma • Computational models • Malignant progression

31.1 Introduction

Since the pioneering work of Murray and Alvord in the 1990s [1–3], there has been an increasing interest for biomathematical modeling of glioma growth. It is remarkable that the proliferation-diffusion model initially proposed by these authors still constitutes the core of elaborated approaches more recently developed. The specific

E. Mandonnet
Hôpital Lariboisière, 2 rue Ambroise Paré, Paris 75010, France
e-mail: mandonnet@mac.com

H. Duffau (ed.), *Diffuse Low-Grade Gliomas in Adults*,
DOI 10.1007/978-3-319-55466-2_31

case of low-grade glioma could be especially favourable for modeling purpose, as their biological behaviour seems to be relatively constant during the "low-grade" phase. Moreover, since «watch and wait » policy has been until recently a standard recommendation in many centers, series of patients radiologically monitored over several years can be retrospectively collected, and serial MRI data sets before any treatment are available for comparison with model predictions.

In this chapter, we will give a brief overview about the proliferation-diffusion equation and explain the difficulties in personalizing the model based on serial MRI images. We will also detail current and future clinical applications, with special emphasis on the key approximations that should be improved in future works. Finally, we will also discuss why the complex problem of modeling the malignant transformation constitutes a real challenge.

31.2 Modeling the Low-Grade Period: The Challenge of an Image-Based Personalized Model

31.2.1 Modeling Proliferation and Migration of Glioma Cells: From a Mathematical Equation to Computational Simulations

On a biological point of view, the behaviour of glioma cells is two fold: proliferation and migration. Mathematical models translate these two characteristics into an equation. The variable in the equation is a coarse-grained tumor cell density (c), which represents the average concentration of tumor cells in each cubic millimeter of the brain. The generic form of the equation, initially introduced in the 1990s [2, 3], is the following:

$$\frac{\partial c}{\partial t} = \rho c + \nabla.\left(D \nabla c\right)$$

that is, evolution with time of tumor cell density (c) at each position in the brain = proliferation (ρc) + diffusion (∇.(D∇c)).

The direct problem consists to compute this equation numerically, on a digital brain template, for given values of ρ and D. The results of the simulations give the evolution over time of maps of tumor cell density (see Fig. 31.1). The template is usually a generic atlas. Over the past decade, advances has been made in integrating a more precise anatomy in this atlas (see Fig. 31.1): whereas the very first templates were built from a 2D CT scan [2, 3], just outlining the brain surface and the ventricles, more recent works are based on 3D-MRI atlases (on which CSF, white and grey matter segmentations are performed [4]), eventually including detailed white matter architecture via DTI sequences [5, 6]. In that case, the D in the equation should read as a tensor of cell diffusion, which can be

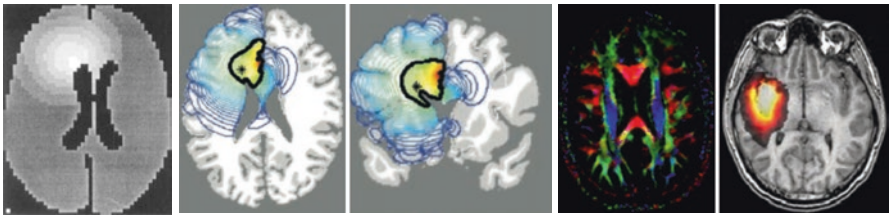

Fig. 31.1 Advances over a decade in the anatomical accuracy of the simulations. The very first templates in 1995 were built from a 2D CT scan [2, 3], just outlining the brain surface and the ventricles. More recent works in 2000 were based on 3D-MRI atlases (on which CSF, *white* and *grey* matter segmentations were performed [4]). Finally, in 2005 detailed *white* matter architecture via DTI sequences was eventually included [6]

built from the tensor of water diffusion, introducing a factor r of anisotropy increase between the two tensors. Diffusion images from an individual healthy volunteer are used [5, 6], but future studies could rely on a tractographic atlas or incorporate own patient DTI MRI. Whatever the elected template, it is of utmost importance that an expert validates its anatomical accuracy. For example, as explained in [6], a wrong segmentation of the subarachnoidal spaces can create artificial bridges of grey matter, especially between the frontal and temporal operculum, leading to unrealistic growth patterns in the simulations. In an effort to correct such inaccuracies, an expert-validated mask of subarachnoidal spaces has been recently built, that greatly improves the veracity of the virtual growth patterns [7].

31.2.2 The Visibility Threshold Hypothesis

The tumoral cell density, which is the variable in the proliferation-diffusion model, is not directly measured on MRI. One has to make the reasonable and simple assumption that the tumor is visible on flair MRI at the condition that tumor cell density is above a given value (visibility threshold). Hence the link between simulated and real tumors relies on the comparison between the thresholded isocontour on cell density maps and the effective contours of the tumor on MRI. Unfortunately, there are very few datas in the literature about the value of this visibility threshold. Only one study correlating histological analysis with hypodensity on CT suggested a value of 8000 cells/mm^3 [1]. Actually, current studies on this topic suggest that the MRI flair hypersignal is not only dependent on the cell density but is also correlated to the intra- and extra-cellular water content [8]. Hence, it should kept in mind that the visibility threshold hypothesis is a strong approximation, and that most of the following results will be based on this assumption.

31.2.3 Model-Based Assessment of Tumor Dynamics

To go a step further towards clinical application, one needs to solve the inverse problem [9], that is to identify the pair of parameters ρ and D specific to a given patient, resulting in the best fit between simulations and a dataset of longitudinal MRIs of the patient. This field of research is also called model personalization. In a first approximate solution of this problem, it can be shown that the proliferation-diffusion equation states that the velocity of expansion of the visible front is a constant given by $2\sqrt{(\rho D)}$ (see Fig. 31.2). In other words, the slope of the linear evolution curve of tumor diameter is given by $4\sqrt{}$ (ρD), where the diameter $d = (2 \times V)^{1/3}$ is computed from the volume V. Note that V is estimated by full 3D-segmentation of the hypersignal on flair sequences. Thus, rather than expressing growth rates in terms of volumetric doubling times (which is the standard method for exponentially growing tumors), one should focus on the slope of diameter growth curves. Recent studies on low-grade glioma kinetics thus enabled to estimate the growth rate of tumor diameter (the so called velocity of diametric expansion, VDE) for individual patients. The average VDE is about 4 mm/year [10], leading to a value of ρD close to 9×10^{-6} mm^2 day^{-2}. Hence this formula is a very simple and convenient way to estimate individually the product ρD from longitudinal MRIs. Finally, quantitative histological analysis could potentially allow to infer

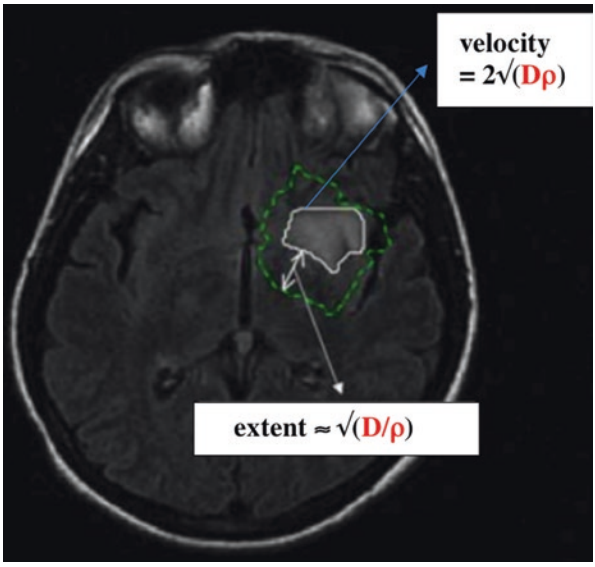

Fig. 31.2 The role of the product Dρ and the ratio D/ρ. The two contours come from the simulation of a patient case. The *thick white* contour corresponds to the threshold of cell density visible on MRI. The velocity of this visible tumor front is given by the formula $2\sqrt{(D\rho)}$. The *dotted line* is the contour corresponding to a cell density five times smaller than the threshold. The extent of the non-visible tumor part is tuned by the ratio D/ρ

the ratio D/ρ: the steepness of the cell density decrease at the tumor margins can be linked to this ratio D/ρ [11]. Surprisingly, there are very few data in the literature on such quantitative histological measures.

More sophisticated tools are currently under development [12, 13], that will allow to estimate the optimized values of parameters minimizing the difference between real and simulated time series of segmented contours. This inverse problem is numerically highly challenging and even not always solvable given the paucity of datas (patients undergo usually two or three MRIs before treatment). At best, one can identify the two products ρD_w and ρD_g, D_w and D_g being the diffusion coefficients in white and grey matter respectively [13]. From this latter study, one can conclude that image-based model personalization will not be achievable in clinical practice, unless one can find an imaging modality that would be indicative of cell density. In this spirit, some authors proposed a method in contrast-enhancing DLGG, assuming that T1-gado and Flair contours correspond to two isolines of distinct visibility thresholds of cell density. They used the two-thresholds method for estimating the ratio D/ρ [14] and the aforementioned method of velocity of diameter expansion to compute the product Dρ. Their results will be discussed in the next paragraph, but it should be kept in mind that there is no evidence that T1-gado and Flair contours are correlated with distinct levels of cell density.

Finally, any image-based personalization implies the segmentations of the tumor on successive images, which is a time consuming task. Hence, this method should be combined in the future with automated tools of segmentation.

31.2.4 Parameters Values for DLGG

For low-grade glioma, values for parameters were initially extrapolated from the values found for high grade glioma and expected to be centered around 0.438/year for ρ and around 4.75 mm^2/year for D [1]. A range of values has been proposed by Harpold et al. [15], with ρ between 1 and 10/year and D between 10 and 100 mm^2/year. In a paper aiming to estimate the individual tumoral birthdates in a large series of DLGG glioma, a range of values for ρ and D was found, which significantly differed from the one previously proposed [16]. A first paper attempted to estimate D and ρ by eyeball fitting of a real patient evolution with simulated images. The best fit was achieved for the values ρ = 0.438/year and D = 3.65 mm^2/year [6], which lies within the domain found by Gerin et al. A very recent study estimated D and ρ on a series of 14 patients with DLGG showing an area of contrast enhancement by using the two-threshold method [17]. While some of the values fall between the expected range, some others were more suggestive of a grade III, as it could have been anticipated given the presence of a contrast enhanced area. All results are summarized on the log-log plot on Fig. 31.3.

For the anisotropic version of the equation, it has been found that the ratio *r* of anisotropy of the tensor cells has to be increased about ten fold compared to the

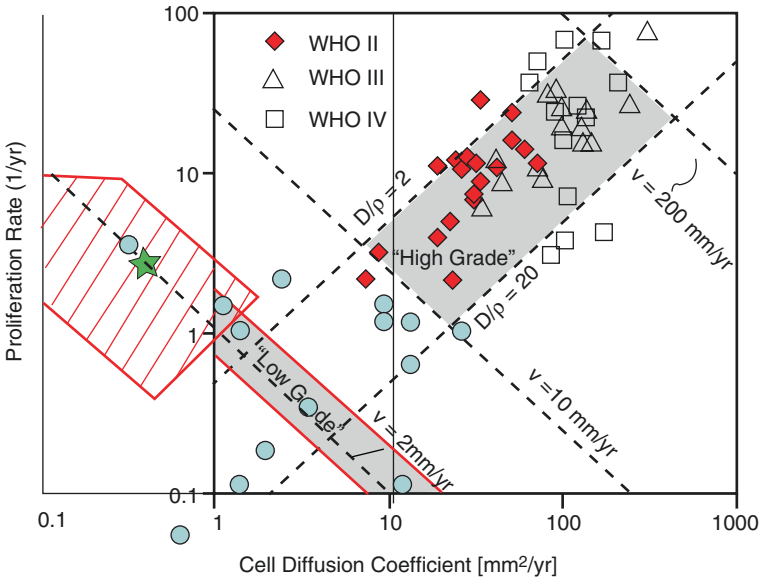

Fig. 31.3 Numerical values of D and ρ in a log-log plot. This diagram has been first discussed by Harpold et al. [15]. The diagonal v = 2 mm/year corresponds to those glioma with a constant product Dρ, with a VDE of 4 mm/year, which is the average value for DLGG. *Red diamonds* correspond to the values found by Ellingson et al. [20] for WHO grade II glioma. Their values are probably irrelevant, as they fall within the expected range for high-grade glioma. The values found by Gerin et al. [16] in the *red dashed area* are correctly centered around the diagonal with a VDE equal to 4 mm/year (i.e. v = 2 mm/year), but with values of the ratio D/ρ smaller than predicted by Harpold et al. Note that the *green star*, corresponding to the DLGG simulation performed by Jbabdi et al. [6], falls within the values found by Gerin et al. The *blue circles* correspond to values found in DLGG with contrast enhancement [17]

anisotropy given by the tensor of water diffusion measured on DTI, reflecting the well known propensity of glioma cells to migrate longitudinally rather than orthogonally to the axonal pathways [6]. This value was indeed needed to reproduce finely the shape of the tumor (which was known to be correlated with the shape of the white matter fasciculus [18]).

31.2.5 Virtual Imaging: Seeing Beyond the Visible

Interestingly, the ratio D/ρ controls the extent of non-visible part of the tumor (i.e. the number of cells located in areas with a cell density lower than the visibility threshold): the higher the ratio D/ρ, the greater the radiologically non-visible part of the tumor [19] (see Fig. 31.3). Although such virtual imaging could be potentially powerful, its practical interest is currently limited, for the two previously mentioned reasons: the lack of reliability of the visibility threshold hypothesis, and the

challenging problem of determining the personalized values of ρ and D for each patient. Should such limitations be overcome, important applications would result, for surgical decision making and for designing radiation therapy margins.

31.3 Future Methods of Model Personalization

31.3.1 Apparent Diffusion Coefficient: The Missing Link Between MRI and Cell Density?

Ellingson et al. proposed in 2011 an elegant and powerful method to estimate 3D individual maps of proliferation and diffusion parameters from at least three longitudinal diffusion weighted sequences [20]. The key assumption is an inverse linear correlation between ADC and cell density (ADC = αc + β, α being negative). These authors have indeed found a negative correlation between cell density and apparent diffusion coefficient, measured from diffusion weighted sequences [21]. Assuming this relation, one can fully inverse the proliferation-diffusion equation, with ρ(x) and D(x) as the unknown variables (ρ(x) and D(x) are the proliferation and diffusion coefficient, that can vary with position x). Three successive ADC maps are nevertheless required, to estimate the time derivatives terms in the equation. The results give nice color maps for proliferation and diffusion, showing spatial changes of these parameters. However, the link between cell density and ADC is not that clear, as ADC changes can be observed in relation to demyelination, edema, and disruption of normal brain architecture [22, 23]. This might explain why the values found by these authors for ρ and D in low-grade glioma are not consistent with the values estimated by the aforementioned approach based on longitudinal morphological follow-up (see Fig. 31.3).

31.3.2 Towards Integration of Longitudinal Multimodality Imaging in the Model

Spectroscopic magnetic resonance imaging also offers a means to estimate cell density and/or proliferation rate of a DLGG, and to get a rough estimate of their spatial variations using multivoxels techniques [24, 25]. Similarly, indices derived from DTI sequences (p and q values, fiber density, …) could also be linked to the cell density in the invasion part outside the flair hypersignal. Hence, this information could potentially be used as inputs for the model personalization process. Promising methods, using a Bayesian framework, are under development to integrate these multimodality imaging and to manage the uncertainty inherent to these experimental data [26]. However, the key point in these methods still relies on the mathematical links between cell density and multimodal imaging parameters

(ADC, Cho/NAA, CNI, p & q in DTI, …), and more efforts should be devoted to their determination.

31.4 Future Applications of Personalized Models

31.4.1 Model-Guided Optimization of Treatment Sequence

Assuming that the inverse problem has been solved—i.e. one is able to personalize the model based on (multimodal) MRI—treatment sequences can be simulated on the virtual tumor of the patient, allowing to select an optimized scheme for each patient. For example, it has been suggested that the benefit of gross total resection for tumors with high values of D/ρ is limited, since a lot of isolated tumor cells would be left even after a radiologically complete resection [27]. One study tested this idea in the context of glioblastoma, and found indeed in a large series of more than 200 patients that no survival benefit of complete resection versus biopsy was observed for patients with high values of D/ρ [28]. However, another study failed to replicate these results [14], proving that the personalization method (based on the hypothesis that T1-gado and Flair extent delineates two isolines of high and low cell density respectively) is not reliable (which does not come as a surprise, since it is well known that flair extent in glioblastoma may result from inflammatory or vasogenic edema, rather than from tumor cells only).

In the same vein, the model would predict that a supra-radical resection of high D/ρ tumors would dramatically increase the delay of recurrence [27]. Identifying these patients would be an essential step, as this information is another parameter to include in the evaluation of the onco-functional balance (see chapter on onco-functional balance by Mandonnet et al.).

Thus, the combined use of patient-specific simulations with tools of preoperative functionally-based prediction of extent of resection [29, 30] could assist the decision making process of surgery versus another oncological treatment (chemotherapy, radiation therapy). To this end, the effect of chemotherapy and radiation therapy should also be included in the model. Some attempts have already been done for modeling radiotherapy in high grade glioma [31, 32], but the validity of such models is not well established. Moreover, the prolonged effect of chemotherapy and radiation therapy in DLGG [33–35] warrants to develop specific models of DLGG response to these treatments [36, 37].

31.4.2 Model-Based Evaluation of Treatment Efficacy

The evaluation of treatment efficacy in DLGG is in itself a real challenge. The usual methodology of evidenced-based medicine that prevails in other fields of oncology, i.e. randomized studies comparing two treatment arms, is inadequate for DLGG

(in their true low-grade period), given the very long survivals of these patients [38]. Moreover, most patients will ultimately also receive the treatment of the other arm, thus precluding to analyze separately the effect of each treatment. Personalized models can play an important role to quantify individual treatment response: for each patient, simulations can act as its own virtual control. Hence, response can be defined at any time as the difference between real (measured) tumor diameter in the patient under study and simulated (predicted) tumor diameter in its untreated virtual clone. In its simplified version, this method consists in comparing the slopes of tumor diameter growth curve before and during treatment.

31.4.3 The Backward Extrapolation

Simulations can also be used to estimate the real biological birthdate of a DLGG, which is anterior to the radiological birthdate estimated by a simple backward linear extrapolation (see chapter on dynamics of DLGG). It can be shown that, within some approximations of the proliferation-diffusion model, a corrective term of 20/v has to be added to the radiological birthdate [16], v being the velocity of diametric expansion (VDE). Applying this principles to a series of 144 patients, it has been found that patients could be classified roughly in two groups: a group of patients with low velocities (v between 1 and 4 mm/year) and a group with high velocities (v between 4 and 8 mm/year). For the low velocity group, patients are about 15 years of age at estimated biological onset, whereas for the high velocity group, patients ages are centered around 25 years of age [16]. Even if these results should be considered very cautiously given the strong underlying hypothesis of the model, they could help to identify different molecular signature of these two groups of tumors and to target age groups for a screening policy (see chapter screening).

31.5 Modeling the Transition Towards Higher-Grade

The transition towards a glioma of higher grade is a somehow unforeseeable event, albeit unavoidable, in the natural history of a LGG. It has been well proven that the greater the initial tumor volume (or its residue after surgery), the higher the risk of imminent anaplastic transformation. Whereas the reference definition of anaplastic transformation is based on the histological criteria of a grade III or IV glioma, it is now widely admitted that it can be also diagnosed by *the appearance in the longitudinal follow-up* of a new contrast-enhanced nodule on T1-gado MRI.

Considering that there is no neoangiogenesis in grade II glioma, we conclude that innate vascularization of the brain parenchyma (probably combined with an optimized metabolic scheme) is able to fulfill the energetic needs of a tumor growing up to 4 mm/year.

On a fundamental point of view, three distinct pathways can lead to the onset of neoangiogenesis (which is the major criteria of malignant transformation):

1. A genetic mutation (or the cumulative effect of several mutations or any changes at molecular scale) can directly drive the building of neo-vessels, irrespective of the hypoxic state of the cells (as it can be observed in the model of tumorigenesis of hemangioblastoma in Von Hippel Lindau patients),
2. Without any additional molecular changes, due to the progressive growth of the tumor, cells can enter an hypoxic environment (decrease of available energetics/oxygen resources per cell), triggering the neo-angiogenic cascade,
3. A genetic mutation (or the cumulative effect of several mutations or any changes at molecular scale) can induce the appearance of a more aggressive cellular behaviour (regarding proliferation rate and/or migration ability), which in turn will lead to an hypoxic focus within the tumor (increase of energetics/oxygen needs per cell).

This three pathways model could explain why longitudinal imaging can fail to anticipate malignant progression. For example, in pathways (1) and (2), the VDE of the tumor measured on the flair images should not increase before the onset of contrast-enhanced nodule. An increase of the VDE should precede the appearance of the contrast-enhanced focus only in pathway (3), as reported by two different studies [39, 40]. Similarly, spectroscopic imaging, which is based on surrogate marker of cell density and/or proliferation (i.e. choline increase, NAA decrease, or Cho/NAA ratio increase), might not be able to predict anaplastic transformation in pathways (1) and (2). In the pathway (1), one would indeed not expect an increase of such markers, as the cellular density and the proliferation rate remain stable despite onset of contrast-enhancement; and in the pathway (2), the increase in cellular density would be not significant enough to be detected by choline and NAA changes. Only in pathway (3) would changes in these compounds be an early marker of anaplastic shift. Of note, recent genomic and epigenomic studies [41–45] give support to pathway (3) in IDH-mutated tumors.

Moreover, this classification could also be of importance regarding treatment selection. It would be expected that surgery is of crucial importance to stop pathway (1), and to a lesser extent to refrain the progression in pathway (2). Pathway (3) would rather require chemotherapy or radiation therapy, as it is likely that the change in cellular behavior has also spread to the cells in the radiologically non-visible part of the tumor.

Interestingly, micro-environment-driven progression has been modeled, within the framework of the proliferation-invasion-hypoxia-necrosis-angiogenesis (PIHNA) model [46]. This model builds upon the proliferation-diffusion model, adding two other populations of cells: hypoxic and necrotic cells, as well as concentration of angiogenic factors and neo-vessels. Normoxic cells evolve towards hypoxic cells at a rate proportional to the concentration of cells and to the proliferation ρ. Hypoxic cells generate angiogenic factors, which in turn lead to an increase of vessels density. The advantage of this model is that it allows quantitative comparison with some histological immunomarkers, like the density of HIF1-α positive cells or the density of

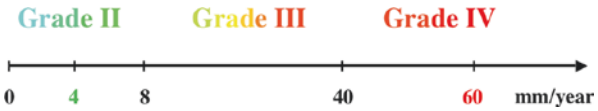

Fig. 31.4 Kinetics classification. The range for grade II is based on the results from Pallud et al. [47]. The range for grade IV comes from the work of Wang et al. [47]. Note that a grade IV kinetics might present at diagnosis with histological characteristics of an histological grade II (at the condition the ratio D/ρ is high, hence the cell density quite low)

VEGF positive cells. The drawback of this approach is that several new parameters are introduced, the values of which are poorly known. As an interesting result, it is shown that a glioma with a product Dρ in the typical range of a glioblastoma (corresponding VDE around 40 mm/year) can exhibit, at initial diagnosis, histological features of a grade II glioma at the condition its ratio D/ρ is very high. Of course, within the next 3 months, histological characteristics of a glioblastoma arise in the simulated tumor. The authors interpret this simulated tumor as a «secondary glioblastoma». We do not share this opinion, as the initial value of D and ρ were typical of a glioblastoma from the beginning. In other words, the tumor is a *de novo* glioblastoma, but due to the high ratio of D/ρ, the cell density was not high enough to generate hypoxic focus triggering the neo-angiogenesis cascade during the first months of growth. In our view, these tumors correspond to «false» grade II (because of high VDE) despite true histological characteristics of grade II: they belong to the 10–15% of histological grade II glioma with an initial VDE higher than 8 mm/year as described in a series of 143 patients [47]. This underlines the importance of a kinetics grading based on VDE, independently of the histological grading (see Fig. 31.4).

31.6 Conclusion

Biomathematical modeling applied to glioma is still in its infancy. But the joined advances of computational modeling and multimodal MRI should offer in a near future powerful tools enabling to build realistic patient-specific virtual tumors. This would open new avenues to develop model-based virtual imaging, and to progress towards the individual optimization of treatment planning.

References

1. Burgess PK, Kulesa PM, Murray JD, Alvord Jr EC. The interaction of growth rates and diffusion coefficients in a three-dimensional mathematical model of gliomas. J Neuropathol Exp Neurol. 1997;56(6):704–13.
2. Tracqui P, Cruywagen GC, Woodward DE, Bartoo GT, Murray JD, Alvord Jr EC. A mathematical model of glioma growth: the effect of chemotherapy on spatio-temporal growth. Cell Prolif. 1995;28(1):17–31.

3. Woodward DE, Cook J, Tracqui P, Cruywagen GC, Murray JD, Alvord Jr EC. A mathematical model of glioma growth: the effect of extent of surgical resection. Cell Prolif. 1996;29(6):269–88.
4. Swanson KR, Alvord Jr EC, Murray JD. A quantitative model for differential motility of gliomas in grey and white matter. Cell Prolif. 2000;33(5):317–29.
5. Clatz O, Sermesant M, Bondiau PY, Delingette H, Warfield SK, Malandain G, Ayache N. Realistic simulation of the 3-D growth of brain tumors in MR images coupling diffusion with biomechanical deformation. IEEE Trans Med Imaging. 2005;24(10):1334–46.
6. Jbabdi S, Mandonnet E, Duffau H, Capelle L, Swanson KR, Pelegrini-Issac M, Guillevin R, Benali H. Simulation of anisotropic growth of low-grade gliomas using diffusion tensor imaging. Magn Reson Med. 2005;54(3):616–24.
7. Amelot A, Stretton E, Delingette H, Ayache N, Froelich S, Mandonnet E. Expert-validated CSF segmentation of MNI atlas enhances accuracy of virtual glioma growth patterns. J Neuro-Oncol. 2015;121(2):381–7.
8. Gerin C, Pallud J, Deroulers C, Varlet P, Oppenheim C, Roux FX, Chretien F, Thomas SR, Grammaticos B, Badoual M. Quantitative characterization of the imaging limits of diffuse low-grade oligodendrogliomas. Neuro-Oncology. 2013;15(10):1379–88.
9. Angelini ED, Clatz O, Mandonnet E, Konukoglu E, Capelle L, Duffau H. Glioma dynamics and computational models: a review of segmentation, registration, and in silico growth algorithms and their clinical applications. Curr Med Imaging Rev. 2007;3(4):425–37.
10. Mandonnet E, Delattre JY, Tanguy ML, Swanson KR, Carpentier AF, Duffau H, Cornu P, Van Effenterre R, Alvord Jr EC, Capelle L. Continuous growth of mean tumor diameter in a subset of grade II gliomas. Ann Neurol. 2003;53(4):524–8.
11. Swanson KR, Bridge C, Murray JD, Alvord Jr EC. Virtual and real brain tumors: using mathematical modeling to quantify glioma growth and invasion. J Neurol Sci. 2003;216(1):1–10.
12. Gholami A, Mang A, Biros G. An inverse problem formulation for parameter estimation of a reaction-diffusion model of low grade gliomas. J Math Biol. 2016;72(1–2):409–33.
13. Konukoglu E, Clatz O, Menze BH, Stieltjes B, Weber MA, Mandonnet E, Delingette H, Ayache N. Image guided personalization of reaction-diffusion type tumor growth models using modified anisotropic eikonal equations. IEEE Trans Med Imaging. 2010;29(1):77–95.
14. Amelot A, Deroulers C, Badoual M, Polivka M, Adle-Biassette H, Houdart E, Carpenter A, Froelich S, Mandonnet E. Surgical decision making from image-based biophysical modeling of glioblastoma: not ready for primetime. Neurosurgery. 2017 Apr 6. doi: 10.1093/neuros/nyw186. [Epub ahead of print].
15. Harpold HL, Alvord Jr EC, Swanson KR. The evolution of mathematical modeling of glioma proliferation and invasion. J Neuropathol Exp Neurol. 2007;66(1):1–9.
16. Gerin C, Pallud J, Grammaticos B, Mandonnet E, Deroulers C, Varlet P, Capelle L, Taillandier L, Bauchet L, Duffau H, Badoual M. Improving the time-machine: estimating date of birth of grade II gliomas. Cell Prolif. 2011;45(1):76–90.
17. Hathout L, Ellingson BM, Cloughesy TF, Pope WB. Patient-specific characterization of the invasiveness and proliferation of low-grade gliomas using serial MR imaging and a mathematical model of tumor growth. Oncol Rep. 2015;33(6):2883–8.
18. Mandonnet E, Capelle L, Duffau H. Extension of paralimbic low grade gliomas: toward an anatomical classification based on white matter invasion patterns. J Neuro-Oncol. 2006;78(2):179–85.
19. Mandonnet E, Pallud J, Clatz O, Taillandier L, Konukoglu E, Duffau H, Capelle L. Computational modeling of the WHO grade II glioma dynamics: principles and applications to management paradigm. Neurosurg Rev. 2008;31(3):263–9.
20. Ellingson BM, LaViolette PS, Rand SD, Malkin MG, Connelly JM, Mueller WM, Prost RW, Schmainda KM. Spatially quantifying microscopic tumor invasion and proliferation using a voxel-wise solution to a glioma growth model and serial diffusion MRI. Magn Reson Med. 2011;65(4):1131–43.

21. Ellingson BM, Malkin MG, Rand SD, Connelly JM, Quinsey C, LaViolette PS, Bedekar DP, Schmainda KM. Validation of functional diffusion maps (fDMs) as a biomarker for human glioma cellularity. J Magn Reson Imaging. 2010;31(3):538–48.
22. Ozturk-Isik E, Pirzkall A, Lamborn KR, Cha S, Chang SM, Nelson SJ. Spatial characteristics of newly diagnosed grade 3 glioma assessed by magnetic resonance metabolic and diffusion tensor imaging. Transl Oncol. 2012;5(1):10–8.
23. Stadlbauer A, Ganslandt O, Buslei R, Hammen T, Gruber S, Moser E, Buchfelder M, Salomonowitz E, Nimsky C. Gliomas: histopathologic evaluation of changes in directionality and magnitude of water diffusion at diffusion-tensor MR imaging. Radiology. 2006;240(3):803–10.
24. Ganslandt O, Stadlbauer A, Fahlbusch R, Kamada K, Buslei R, Blumcke I, Moser E, Nimsky C. Proton magnetic resonance spectroscopic imaging integrated into image-guided surgery: correlation to standard magnetic resonance imaging and tumor cell density. Neurosurgery. 2005;56(2 Supp l):291–8. discussion 291-8
25. McKnight TR, Lamborn KR, Love TD, Berger MS, Chang S, Dillon WP, Bollen A, Nelson SJ. Correlation of magnetic resonance spectroscopic and growth characteristics within Grades II and III gliomas. J Neurosurg. 2007;106(4):660–6.
26. Menze BH, Van Leemput K, Honkela A, Konukoglu E, Weber MA, Ayache N, Golland P. A generative approach for image-based modeling of tumor growth. Inf Process Med Imaging. 2011;22:735–47.
27. Swanson KR, Alvord Jr EC, Murray JD. Virtual resection of gliomas: effect of extent of resection on recurrence. Math Comput Model. 2003;37:1177–90.
28. Baldock AL, Ahn S, Rockne R, Johnston S, Neal M, Corwin D, Clark-Swanson K, Sterin G, Trister AD, Malone H, Ebiana V, Sonabend AM, Mrugala M, Rockhill JK, Silbergeld DL, Lai A, Cloughesy T, McKhann 2nd GM, Bruce JN, Rostomily RC, Canoll P, Swanson KR. Patient-specific metrics of invasiveness reveal significant prognostic benefit of resection in a predictable subset of gliomas. PLoS One. 2014;9(10):e99057.
29. Ius T, Angelini E, Thiebaut de Schotten M, Mandonnet E, Duffau H. Evidence for potentials and limitations of brain plasticity using an atlas of functional resectability of WHO grade II gliomas: towards a “minimal common brain”. NeuroImage. 2011;56(3): 992–1000.
30. Mandonnet E, Jbabdi S, Taillandier L, Galanaud D, Benali H, Capelle L, Duffau H. Preoperative estimation of residual volume for WHO grade II glioma resected with intraoperative functional mapping. Neuro-Oncology. 2007;9(1):63–9.
31. Corwin D, Holdsworth C, Rockne RC, Trister AD, Mrugala MM, Rockhill JK, Stewart RD, Phillips M, Swanson KR. Toward patient-specific, biologically optimized radiation therapy plans for the treatment of glioblastoma. PLoS One. 2013;8(11):e79115.
32. Unkelbach J, Menze BH, Konukoglu E, Dittmann F, Ayache N, Shih HA. Radiotherapy planning for glioblastoma based on a tumor growth model: implications for spatial dose redistribution. Phys Med Biol. 2014;59(3):771–89.
33. Pallud J, Llitjos JF, Dhermain F, Varlet P, Dezamis E, Devaux B, Souillard-Scemama R, Sanai N, Koziak M, Page P, Schlienger M, Daumas-Duport C, Meder JF, Oppenheim C, Roux FX. Dynamic imaging response following radiation therapy predicts long-term outcomes for diffuse low-grade gliomas. Neuro-Oncology. 2012;14(4):496–505.
34. Peyre M, Cartalat-Carel S, Meyronet D, Ricard D, Jouvet A, Pallud J, Mokhtari K, Guyotat J, Jouanneau E, Sunyach MP, Frappaz D, Honnorat J, Ducray F. Prolonged response without prolonged chemotherapy: a lesson from PCV chemotherapy in low-grade gliomas. Neuro Oncol. 2010;12(10):1078–82.
35. Ricard D, Kaloshi G, Amiel-Benouaich A, Lejeune J, Marie Y, Mandonnet E, Kujas M, Mokhtari K, Taillibert S, Laigle-Donadey F, Carpentier AF, Omuro A, Capelle L, Duffau H, Cornu P, Guillevin R, Sanson M, Hoang-Xuan K, Delattre JY. Dynamic history of low-grade gliomas before and after temozolomide treatment. Ann Neurol. 2007;61(5):484–90.

36. Badoual M, Gerin C, Deroulers C, Grammaticos B, Llitjos JF, Oppenheim C, Varlet P, Pallud J. Oedema-based model for diffuse low-grade gliomas: application to clinical cases under radiotherapy. Cell Prolif. 2014;47(4):369–80.
37. Ribba B, Kaloshi G, Peyre M, Ricard D, Calvez V, Tod M, Čajavec-Bernard B, Idbaih A, Psimaras D, Dainese L, Pallud J, Cartalat-Carel S, Delattre JY, Honnorat J, Grenier E, Ducray F. A tumor growth inhibition model for low-grade glioma treated with chemotherapy or radiotherapy. Clin Cancer Res. 2012;18(18):5071–80.
38. Mandonnet E, Duffau H, Bauchet L. A new tool for grade II glioma studies: plotting cumulative time with quality of life versus time to malignant transformation. J Neuro-Oncol. 2011;106(1):213–5.
39. Hathout L, Pope WB, Lai A, Nghiemphu PL, Cloughesy TF, Ellingson BM. Radial expansion rates and tumor growth kinetics predict malignant transformation in contrast-enhancing low-grade diffuse astrocytoma. CNS Oncol. 2015;4(4):247–56.
40. Rees J, Watt H, Jager HR, Benton C, Tozer D, Tofts P, Waldman A. Volumes and growth rates of untreated adult low-grade gliomas indicate risk of early malignant transformation. Eur J Radiol. 2009;72(1):54–64.
41. Bai H, Harmanci AS, Erson-Omay EZ, Li J, Coskun S, Simon M, Krischek B, Ozduman K, Omay SB, Sorensen EA, Turcan S, Bakirciglu M, Carrion-Grant G, Murray PB, Clark VE, Ercan-Sencicek AG, Knight J, Sencar L, Altinok S, Kaulen LD, Gulez B, Timmer M, Schramm J, Mishra-Gorur K, Henegariu O, Moliterno J, Louvi A, Chan TA, Tannheimer SL, Pamir MN, Vortmeyer AO, Bilguvar K, Yasuno K, Gunel M. Integrated genomic characterization of IDH1-mutant glioma malignant progression. Nat Genet. 2016;48(1):59–66.
42. Ceccarelli M, Barthel FP, Malta TM, Sabedot TS, Salama SR, Murray BA, Morozova O, Newton Y, Radenbaugh A, Pagnotta SM, Anjum S, Wang J, Manyam G, Zoppoli P, Ling S, Rao AA, Grifford M, Cherniack AD, Zhang H, Poisson L, Carlotti Jr CG, Tirapelli DP, Rao A, Mikkelsen T, Lau CC, Yung WK, Rabadan R, Huse J, Brat DJ, Lehman NL, Barnholtz-Sloan JS, Zheng S, Hess K, Rao G, Meyerson M, Beroukhim R, Cooper L, Akbani R, Wrensch M, Haussler D, Aldape KD, Laird PW, Gutmann DH, Noushmehr H, Iavarone A, Verhaak RG. Molecular profiling reveals biologically discrete subsets and pathways of progression in diffuse glioma. Cell. 2016;164(3):550–63.
43. Mazor T, Pankov A, Johnson BE, Hong C, Hamilton EG, Bell RJ, Smirnov IV, Reis GF, Phillips JJ, Barnes MJ, Idbaih A, Alentorn A, Kloezeman JJ, Lamfers ML, Bollen AW, Taylor BS, Molinaro AM, Olshen AB, Chang SM, Song JS, Costello JF. DNA methylation and somatic mutations converge on the cell cycle and define similar evolutionary histories in brain tumors. Cancer Cell. 2015;28(3):307–17.
44. Park CK, Park I, Lee S, Sun CH, Koh Y, Park SH, Kim JE, Yun H, Lee SH. Genomic dynamics associated with malignant transformation in IDH1 mutated gliomas. Oncotarget. 2015;6(41):43653–66.
45. Suzuki H, Aoki K, Chiba K, Sato Y, Shiozawa Y, Shiraishi Y, Shimamura T, Niida A, Motomura K, Ohka F, Yamamoto T, Tanahashi K, Ranjit M, Wakabayashi T, Yoshizato T, Kataoka K, Yoshida K, Nagata Y, Sato-Otsubo A, Tanaka H, Sanada M, Kondo Y, Nakamura H, Mizoguchi M, Abe T, Muragaki Y, Watanabe R, Ito I, Miyano S, Natsume A, Ogawa S. Mutational landscape and clonal architecture in grade II and III gliomas. Nat Genet. 2015;47(5):458–68.
46. Swanson KR, Rockne RC, Claridge J, Chaplain MA, Alvord Jr EC, Anderson AR. Quantifying the role of angiogenesis in malignant progression of gliomas: in silico modeling integrates imaging and histology. Cancer Res. 2011;71(24):7366–75.
47. Pallud J, Mandonnet E, Duffau H, Kujas M, Guillevin R, Galanaud D, Taillandier L, Capelle L. Prognostic value of initial magnetic resonance imaging growth rates for World Health Organization grade II gliomas. Ann Neurol. 2006;60(3):380–3.
48. Wang CH, Rockhill JK, Mrugala M, Peacock DL, Lai A, Jusenius K, Wardlaw JM, Cloughesy T, Spence AM, Rockne R, Alvord Jr EC, Swanson KR. Prognostic significance of growth kinetics in newly diagnosed glioblastomas revealed by combining serial imaging with a novel biomathematical model. Cancer Res. 2009;69(23):9133–40.